nature geoscience

Article

https://doi.org/10.1038/s41561-022-01071-5

# Formation of oxidized sulfur-rich magmas in Neoarchaean subduction zones

Received: 4 May 2022

Accepted: 12 October 2022

Published online: 28 November 2022

Check for updates

Xuyang Meng[1,2,5] ✉, Adam C. Simon[2] ✉, Jackie M. Kleinsasser[2], David R. Mole[3,4], Daniel J. Kontak[1], Pedro J. Jugo[1], Jingwen Mao[5] ✉ & Jeremy P. Richards[1,6]

Oxidized, sulfur-rich arc magmas are ubiquitous in modern subduction-zone environments. These magmas are thought to form when the fluids released during prograde metamorphism of subducting oceanic crust and overlying sediments oxidize and hydrate the asthenospheric mantle. In contrast, Archaean arc-type magmas are thought to be relatively reduced and sulfur poor, owing to the lower concentrations of marine sulfate and limited oxidative seafloor alteration in the anoxic ocean before the Great Oxidation Event some 2.4 billion years ago (Ga). Here we measure the total sulfur concentration and relative abundances of $S^{6+}$, $S^{4+}$ and $S^{2-}$ in zircon-hosted apatite grains from sodic and potassic intrusive rocks from the ~2.7 Ga southeastern Superior Province, Canada. We find that, rather than being reduced and sulfur poor, the sulfur budget of the Neoarchaean magmas was dominated by $S^{6+}$ and abruptly increased to concentrations comparable to Phanerozoic arc magmas following the interpreted onset of subduction at approximately 2.7 Ga, coincident with the first global pulse of crust generation. These findings indicate that oxidized, sulfur-rich magmas formed in subduction zones independent of ocean redox state and could have influenced oceanic–atmospheric and metallogenic evolution in the Neoarchaean.

Volatile sulfate ($S^{6+}$) is the dominant sulfur species in oxidized silicate melts and exerts significant influence on volcanic $SO_2$ emission[1,2], magmatic hydrothermal mineral deposit formation[3] and, plausibly, the onset of atmospheric oxygenation via bacterial sulfate reduction[4]. Phanerozoic oxidized sulfur-rich arc magmas typically formed from flux melting of the asthenospheric mantle during subduction of seawater-altered oceanic crust and overlying sediments that carried sulfate and/or ferric iron into the sub-arc mantle[5–8]. The ubiquitous presence of oxidized sulfur-rich magmas in the Phanerozoic is consistent with extensive deep-ocean oxygenation[7,9]. On the contrary, Archaean arc magmas are hypothesized to be sulfur poor owing to the absence of mass transfer of oxidized materials into the ancient sub-arc mantle[9,10]. However, this hypothesis remains poorly tested with limited constraints on the oxidation states and concentrations of sulfur in Archaean magmas. Recent studies have identified local presence of relatively oxidized sulfur-rich magmas in the Palaeoproterozoic and the Archaean[11,12], casting doubt on whether deep-ocean oxygenation is fundamental to forming sulfate-rich magmas in subduction-zone environments.

To resolve this issue, we systematically measured the oxidation states and concentrations of sulfur in samples of arc-type magmas in the Neoarchaean southeastern Superior Province, Canada. The southeastern Superior Province, which is dominated by the Abitibi–Wawa greenstone belt, is regarded as one of the earliest and best-exposed

[1]Mineral Exploration Research Centre, Harquail School of Earth Sciences, Laurentian University, Sudbury, Ontario, Canada. [2]Department of Earth and Environmental Sciences, University of Michigan, Ann Arbor, MI, USA. [3]Research School of Earth Sciences, Australian National University, Canberra, Australian Capital Territory, Australia. [4]Centre for Exploration Targeting, School of Earth Sciences, The University of Western Australia, Perth, Western Australia, Australia. [5]Present address: China University of Geosciences, Beijing, China. [6]Deceased: Jeremy P. Richards. ✉e-mail: xuyangm@umich.edu; simonac@umich.edu; jingwenmao@263.net

https://doi.org/10.1038/s41561-022-01071-5

examples for arc formation and accretion 2.7 billion years ago (Ga) (ref. [13]). The relatively low marine sulfate contents (<200 μM) and less oxidized hydrothermally altered seafloor[14,15], even if upon their recycling into the mantle, had probably not allowed the slab-derived fluids to oxidize the sub-arc mantle at that time. The southeastern Superior Province records the evolution from sodic to potassic magmatism broadly similar to other cratons, possibly reflecting a change in global geodynamic setting (that is, onset of subduction–collision cycle)[16,17]. Post-emplacement metamorphism of the igneous rocks in the southeastern Superior Province[18] requires that any constraints for the original composition and primary oxidation state of the magmas be determined using phases not affected by metamorphism.

Here we circumvented that challenge by measuring the abundances and different oxidation states of sulfur in primary igneous apatite—$Ca_5(PO_4)_3(OH, F, Cl)$—hosted by primary igneous zircon that is resistant to post-crystallization modification. The poor ability of zircon to incorporate sulfur (<2 ppm) in its structure prevents post-entrapment diffusion of sulfur out of the apatite inclusion[19,20]. We used synchrotron-based micro X-ray absorption near-edge structure spectroscopy at S K-edge (μ-XANES) to measure the ratios of $S^{6+}$ to total S ($S^{6+} + S^{4+} + S^{2-}$) and electron probe micro-analyser (EPMA) to measure sulfur concentrations of zircon-hosted apatite inclusions from intrusive rocks mainly in the southeastern Superior Province. The integrated $S^{6+} / \Sigma(S^{6+} + S^{4+} + S^{2-})$ ratios, reported as $S^{6+} / \Sigma S$, constrain the redox states of the sodic and potassic magmas during the ~75 million year evolution of the southeastern Superior Province.

## Tectonomagmatic evolution of southeastern Superior Province

The southeastern Superior Province (dominated by the Abitibi–Wawa greenstone belt) is marked by east–west-elongated terranes juxtaposed along fold-and-thrust belts (Extended Data Fig. 1a) that are interpreted by seismic reflection profiling as palaeo-subduction zones (refs. [12,21] and references therein). The southeastern Superior Province preserves plutonic rocks that formed between 2,750 million years ago (Ma) and 2,670 Ma in a tectonic setting interpreted to have evolved from (1) 'plume-arc' interaction or episodic short-term subduction under a broadly extensional environment before ~2,705 Ma, (2) to persistent northward subduction at ~2,705–2,685 Ma and (3) continental collision and transform motion at 2,685–2,670 Ma (refs. [12,18,22,23] and references therein). The presence of submarine volcanic assemblages (for example, pillow basalts) and deep-water flysch-like sedimentary rocks have been interpreted as evidence that the subaerial landmass emerged as a result of crustal thickening and uplift until ~2,685 Ma (refs. [12,22]).

The plutonic rocks evolved from sodic to potassic over the tectonic evolution (Fig. 1), including (1) pre-tectonic, syn-volcanic sodic-enriched tonalite–trondhjemite–diorite originating from partial melting of hydrated mafic source at variable depths, (2) early syn-tectonic tonalite–granodiorite derived from melting of a subducted slab, (3) syn- to late-tectonic sanukitoid (*sensu lato*) sourced from a metasomatized mantle to (4) late-tectonic alkalic rocks derived from remelting of metasomatically $CO_2$-enriched mantle sources[12,18,24–26]. The pre-tectonic sodic rocks were constrained to have been emplaced at 300–700 MPa (locally at ~100 MPa), whereas the early syn-tectonic tonalite–granodiorite and the younger potassic and sanukitoid rocks emplaced at 100–400 MPa (refs. [12,24,27–30]). The rocks commonly underwent metamorphism up to greenschist facies and locally lower amphibolite facies and underwent extensive deformation and hydrothermal alteration.

## Estimates of magmatic oxygen fugacity and sulfur contents

Zircon grains from the studied samples typically exhibit oscillatory or sector zoning (Extended Data Fig. 2), reflecting primary features that eliminate post-crystallization metamorphism and/or alteration of their

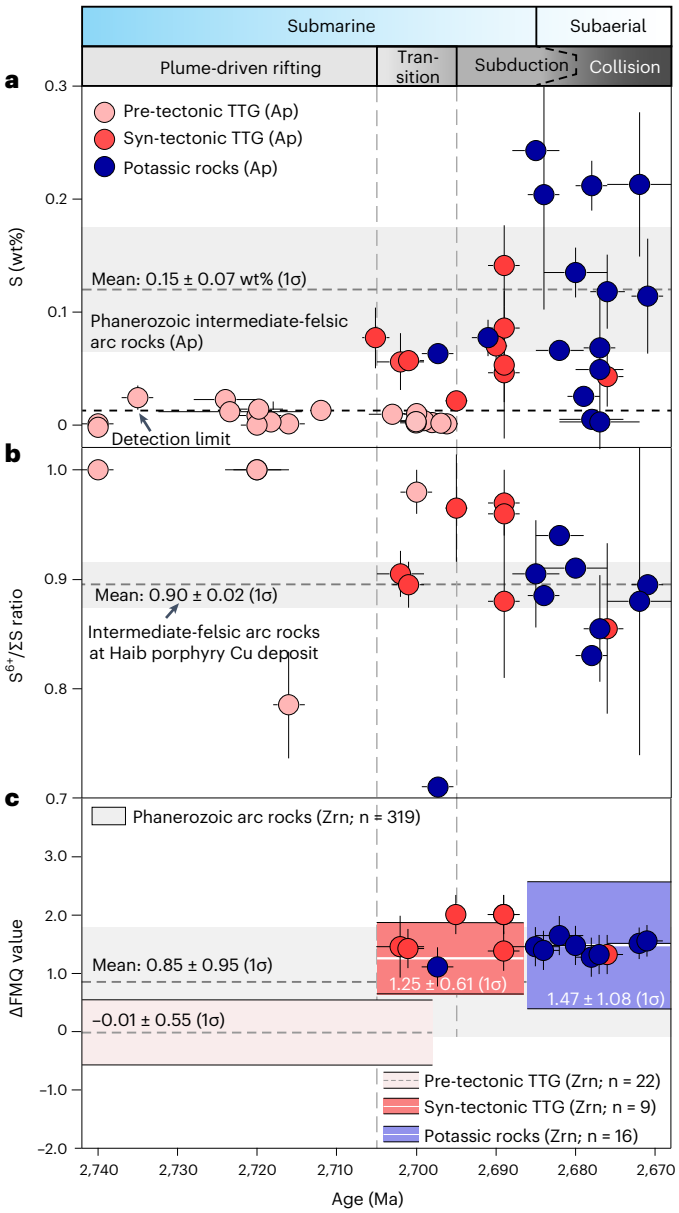


**Fig. 1 | The time-constrained apatite sulfur data and the estimated oxygen fugacity values for representative intrusive rocks from the southeastern Superior Province. a**, Apatite sulfur contents. **b**, Integrated $S^{6+} / \Sigma S$ peak area ratios. **c**, ΔFMQ values. The detection limit of the sulfur content is 0.012 wt%. The tectonic interpretation is from refs. [12,22], whereas the timing of transition from the submarine to subaerial surface environments is estimated based on the onset of subaerial alluvial–fluvial sedimentation[61]. The average apatite sulfur contents for Phanerozoic arc-related intermediate-felsic rocks (**a**) and the average apatite $S^{6+} / \Sigma S$ ratio for the Haib rocks (**b**) are from ref. [11]. The average ΔFMQ values from zircon geochemistry in **c** are estimated using the method of ref. [62] and are presented as mean values ± SD (1σ). Error bars for the apatite sulfur data, ΔFMQ values and the U–Pb ages indicate 1σ, 1σ and 2SE, respectively. Extended Data Fig. 1a provides the simplified geologic map. Supplementary Table 1 provides sample locations and descriptions and the compiled zircon geochronological results. The EPMA analyses for the apatite grains are provided in Supplementary Table 2. The zircon trace element data for the studied intrusive rocks in southeastern Superior Province are compiled from refs. [11,22], whereas those for Phanerozoic intermediate-felsic arc rocks are compiled from literature in Supplementary Table 3. *n* represents numbers of rock samples. The horizonal dashed lines along the center of the error bands represent the mean values. Abbreviations: Ap = apatite, Zrn = zircon, SD = standard deviation, SE = standard error, TTG = Tonalite-trondhjemite-granodiorite.

https://doi.org/10.1038/s41561-022-01071-5

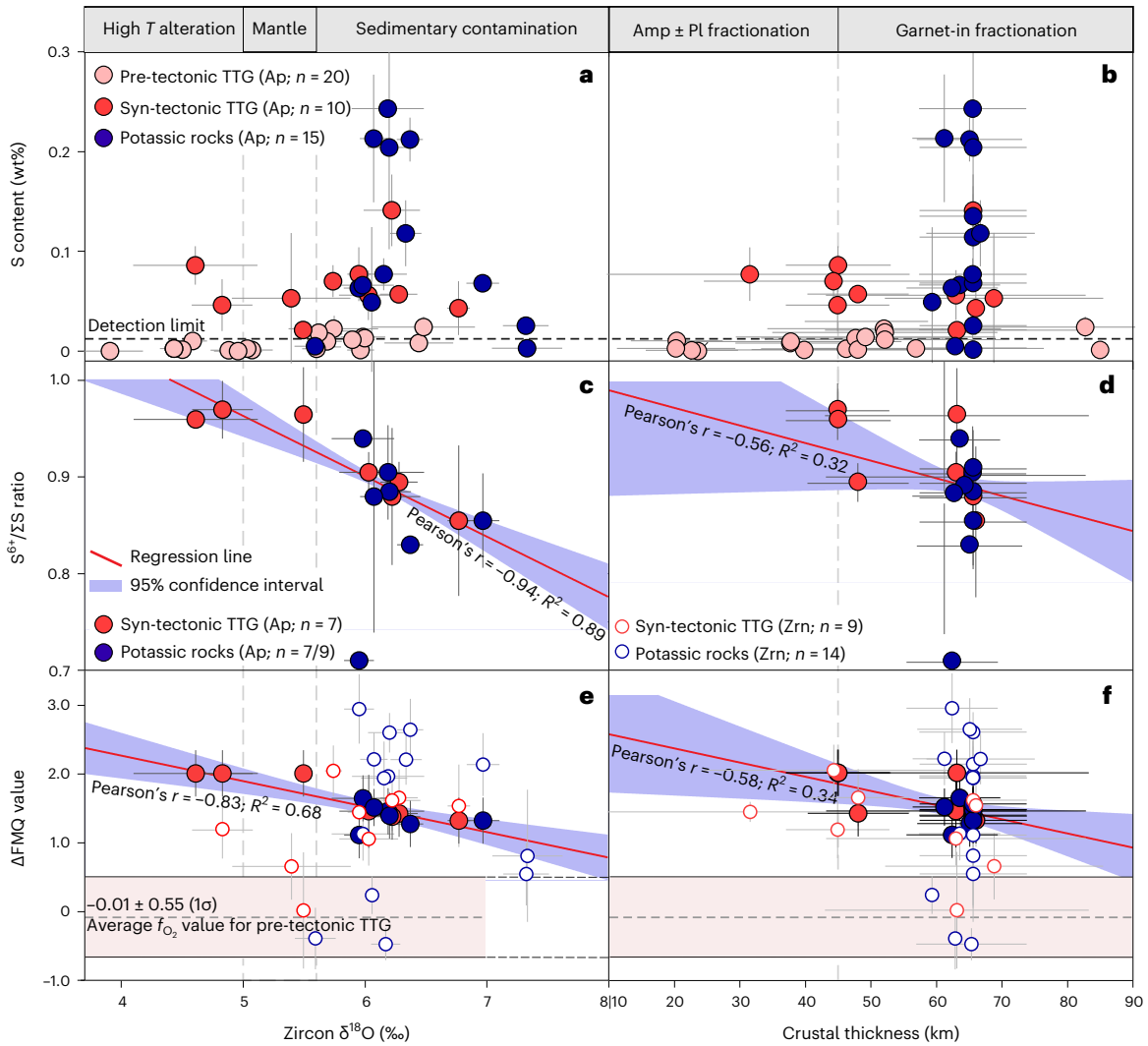


**Fig. 2 | Plots of apatite sulfur contents, sulfate ratios and the magmatic $f_{O_2}$ values against zircon $^{18}$O stable isotope ratios and the crustal thickness.** **a**,**b**, Apatite sulfur contents versus zircon $\delta^{18}O$ values and the crustal thickness. **c**,**d**, Apatite $S^{6+}/\Sigma S$ ratios versus zircon $\delta^{18}O$ values and the crustal thickness. **e**,**f**, ΔFMQ values versus zircon $\delta^{18}O$ values and the crustal thickness. The zircon O isotope and ΔFMQ values are recalculated using datasets filtered from refs. [12,22] (screening criteria and the results in Supplementary Table 1). Crustal thickness estimation provided in Methods and Supplementary Table 1, and Extended Data Fig. 6. The red lines and light blue error bands in **c**–**f** represent regression lines and 95% confidence intervals, respectively. The best-fit regression lines in **e** and **f** are for the ΔFMQ values estimated using the S in apatite oxybarometer. The ΔFMQ values were estimated using the zircon Ce–Ti–$U_i$ oxybarometer[62] ($U_i$ = initial U content in zircon at the time of crystallization) with a high standard error (0.6 log units) are plotted for comparison. The mantle value for zircon O isotopes is 5.3 ± 0.3‰ (1σ) (ref. [63]). The crustal thickness favoured amphibole ± plagioclase and garnet-in fractionation are estimated based on pressures from experimental results (assuming liquidus temperature of ~1,000 °C at $H_2O$ undersaturated condition) compiled in ref. [42]. Error bars indicate standard deviations. The average zircon ΔFMQ value for the pre-tectonic TTG rocks is presented as mean value ± SD. *n* represents numbers of rock samples. The vertical dashed lines are used to divide different regions for zircon O isotopic values and crustal thickness. The horizontal dashed lines along the center of the pink error bars in panels **e** and **f** represent the mean values of magmatic $f_{O_2}$ values. Abbreviations: Amp = amphibole, Ap = apatite, Pl = plagioclase, Zrn = zircon, T = temperature.

apatite inclusions. Most of the studied apatite inclusions are equant to sub-equant and not intergrown with other silicate minerals (Extended Data Fig. 2). These observations are consistent with crystallization of the apatite inclusions at near-liquidus, near-equilibrium conditions. Apatite saturation thermometry[31] yielded an average temperature of crystallization of 898 ± 54 °C (1σ) for apatite inclusions from the sodic and potassic rocks (Extended Data Fig. 3). The elevated apatite saturation temperature relative to zircon saturation (741 ± 54 °C; 1σ) (ref. [32]) and Ti in zircon temperatures (764 ± 30 °C; 1σ; Extended Data Fig. 3)[33] are consistent with the observation of earlier crystallization of apatite than the zircon.

Figure 1a shows that the sulfur concentrations of the primary apatite increase by a factor of five from ~0.01 wt% (that is, below the detection limit) for syn-volcanic sodic granitoids to 0.06 ± 0.03 wt% and 0.11 ± 0.08 wt% for syn-tectonic tonalite-trondhjemite-granodiorite (TTG) and syn- to late-tectonic potassic rocks. The sulfur concentrations of zircon-hosted apatite inclusions from the syn- to late-tectonic granitoids in the southeastern Superior Province reported here are similar to the sulfur concentrations reported for apatite in Phanerozoic arc magmas (Fig. 1a)[11]. The apatite grains analysed in this study yielded statistically similar $S^{6+}/\Sigma S$ values of 0.95 ± 0.09 (1σ) and 0.92 ± 0.05 (1σ) for syn-volcanic and early syn-tectonic TTG rocks and slightly decrease to 0.87 ± 0.07 (1σ) for syn- to late-tectonic potassic rocks (1σ; Fig. 1b and Extended Data Fig. 4).

The partitioning behaviour of sulfur between apatite and silicate melt varies systematically as a function of magmatic oxygen fugacity

https://doi.org/10.1038/s41561-022-01071-5

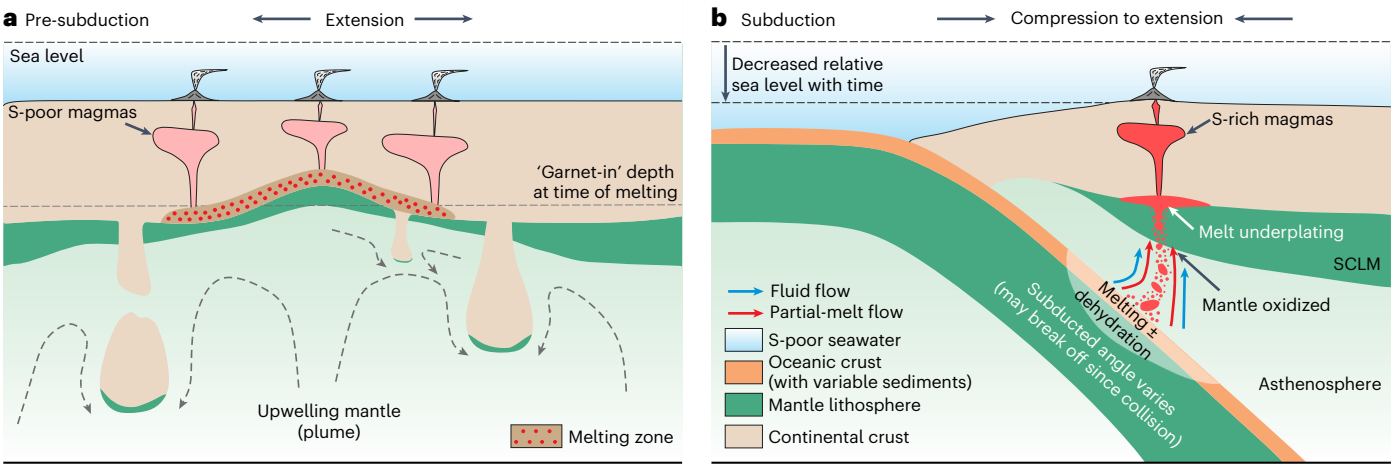


**Fig. 3 | Schematic cartoon models illustrating two main contrasting tectonomagmatic regimes operated in the southeastern Superior Province (not to scale). a**, Sulfur-poor sodic TTG magmas formed from sulfur-poor hydrated lower crust at variable depths during lithospheric extension and dripping, modified from refs. [22,64]. The tectonic regime is inferred in ref. [22], although short-term near-vertical subduction might also operate[23]. **b**, Relatively oxidized sulfur-rich TTG and subsequent potassic magmas formed from relatively oxidized sub-arc mantle metasomatized during subduction of the oceanic lithosphere that was hydrothermally altered in a sulfate-poor, anoxic ocean, modified from ref. [36]. The angle of the subduction remains debated with flat to steep proposed[21,22,26]. The relative sea level decreased with crustal thickening, with extensive subaerial landmasses emerging since the collision. Remelting of the modified mantle lithosphere may take place during asthenospheric upwelling triggered by post-collision slab breakoff (the exact process not depicted here for simplification). Note that **a** and **b** may operate coevally in the southeastern Superior Province (for example, at ~2.7 Ga transition period). SCLM = subcontinental lithosphere mantle.

($f_{O_2}$) and is not suggested to change with bulk melt composition (from basaltic to rhyolitic)[34]. Using the S in apatite oxybarometer[34] experimentally calibrated for hydrous mafic silicate melt at 1,000 °C and 300 MPa (details of P–T correction in Methods), the integrated $S^{6+}/\Sigma S$ peak area ratios reported here yielded statistically comparable magmatic $f_{O_2}$ values of ΔFMQ + 1.66 ± 0.33 (1σ) and +1.42 ± 0.16 (1σ) for the syn-tectonic tonalite–granodiorite and syn- to late-tectonic potassic rocks, respectively; ΔFMQ is the fayalite–magnetite–quartz redox buffer. These results are consistent with but are more precise than the magmatic $f_{O_2}$ values estimated using previously published zircon geochemistry[12,22] for the studied samples from the southeastern Superior Province (Fig. 1c).

A $D_S^{ap/m}$ model[11], where $D$ is the partition coefficient for S between apatite (ap) and silicate melt (m), based on published apatite/melt sulfur partition coefficient values as functions of magmatic $f_{O_2}$ and temperature[34,35] is used to calculate primary melt sulfur concentrations that range from 0.04 ± 0.03 to 0.07 ± 0.05 wt% (1σ) for syn-tectonic TTG rocks and 0.08 ± 0.06 to 0.14 ± 0.11 wt% (1σ) for the syn- to late-potassic rocks (Supplementary Table 1). The magmatic $f_{O_2}$ and melt sulfur concentrations reported here for the arc-type intermediate-felsic magmas in the southeastern Superior Province are consistent with the Phanerozoic analogues[11].

## Origin of oxidized sulfur-rich magmas in the Archaean

Oxidized sulfur-rich magmas in Phanerozoic arc-related settings are generally accepted to have formed as a result of subduction-induced prograde metamorphism of hydrated oceanic lithosphere and overlying oxidized sediments from which a supercritical H–O–S–C–Cl fluid evolves and transfers oxidizing components such as $Fe^{3+}$ and $S^{6+}$ into the forearc mantle wedge[5,36]. Deep-ocean oxygenation and the formation of seafloor sulfate requires atmospheric oxygenation and is thought not to have occurred until the Neoproterozoic[9,15]. The low marine sulfate concentrations (<200 μM) and less oxidized hydrothermally altered seafloor in the Archaean predict that arc-related magmas formed during that time should have been relatively reduced (that is, low $S^{6+}/\Sigma S$) and sulfur poor.

However, the time series data reported here for the ~2.7 Ga intrusive rocks in the southeastern Superior Province contradict that prediction in two aspects. First, igneous apatite from the pre-tectonic sodic plutonic rocks yielded high $S^{6+}/\Sigma S$ ratios and low sulfur contents (Figs. 1 and 2), indicating a minor amount of oxidized sulfur (that is, $S^{6+}$) in the silicate melts. The low melt sulfur contents may indicate a sulfur-poor source region (Fig. 3a), whereas the dominance of $S^{6+}$ in the melts may be attributed to the increased redox state of sulfur-poor felsic magmas by degassing during their ascent[37,38] or that the sulfide–sulfate transition is shifted to lower ΔFMQ values for Fe-poor haplo-trondhjemitic liquid[39]. The low magmatic $f_{O_2}$ values estimated from zircon geochemistry are more consistent with the shift of sulfide–sulfate transition for the magmas to reduced $f_{O_2}$ space that can be interpreted as a result of low $H_2O$ contents in melts influencing their rheological properties and phase equilibria[40].

Second, and more intriguingly, the belt-scale arc magmas emplaced after ~2,705 Ma incorporate sulfur as predominantly sulfate, comparable to their Phanerozoic analogues[2,11]. We interpret this to reflect either a relatively oxidized mantle wedge caused by subduction-initiated flux melting[5] or increased melt sulfate solubility by magmatic auto-oxidation during differentiation (that is, garnet fractionation) in a thick crust[41]. However, both crustal thickness and crustal recycling increase with progressive subduction and collision as supported by the increase of zircon $\delta^{18}O$ values with the estimated crustal thickness (Extended Data Fig. 5). We therefore highlight the spatio-temporal relationship of subduction with crustal recycling and thickening.

To distinguish between these plausible scenarios, the concentrations of sulfur in apatite are plotted against the $\delta^{18}O$ values of their zircon host (Fig. 2a) and the estimated crustal thickness (Fig. 2b) that are proxies of the degrees of crustal recycling (that is, via subducting slab) and garnet fractionation (favoured in >45 km crustal levels[42]), respectively. Figure 2 shows that most of the sulfur-rich apatite grains crystallized from silicate melts with elevated zircon $\delta^{18}O$ values relative to the mantle value (Fig. 2a) and yielded high $S^{6+}/\Sigma S$ ratios consistent with oxidized magmatic environments (ΔFMQ + 1 to +2; Fig. 2c,e).

The immediate occurrence of sulfate-rich apatite at ~2.7 Ga is consistent with the interpreted onset of subduction in the southeastern Superior Province (Fig. 1a), possibly reflecting a close relationship between the subduction initiation process and formation of oxidized sulfur-rich magmas (Fig. 3b).

In addition, the sulfate-rich apatite can crystallize from silicate melts originating from source regions at variable depths, including <45 km where substantial garnet fractionation is unfavoured (Fig. 2b,d). The absence of or weak negative correlation between crustal thickness and magmatic $f_{O_2}$ values (Fig. 2f) further evidences that garnet fractionation during crustal thickening does not increase the magmatic $f_{O_2}$ values. We note that the crustal thickness for the TTG rocks reported here may be overestimated considering the recent studies that indicate 'high-pressure' TTG magmas can form from melting of hydrated basalts at <40 km depth[43–45]. Nonetheless, these more recent models for the formation of TTG magmas support our interpretation that garnet fractionation in a thick crust was not the fundamental cause of the high $S^{6+}/\Sigma S$ ratios and sulfur concentrations of apatite reported here.

The strong negative correlations of $S^{6+}/\Sigma S$ ratios of apatite and the magmatic $f_{O_2}$ values with $\delta^{18}O$ values for zircon that are independent of bulk composition (Fig. 2c,e) plausibly reflect recycling of relatively reduced sediments to the sub-arc mantle in the Archaean and/or crustal assimilation during magma ascent. The fact that zircon separates from each of the studied samples generally lack xenocrysts and yielded narrow ranges of $\delta^{18}O$ and εHf(t) values (ε, epsilon; t, time (the crystallization ages of the zircon grains)) (summary in Supplementary Table 1) suggests insignificant assimilation of crustal materials during magma ascent. The pre-tectonic sodic plutonic rocks that predominate the >2.7 Ga crust in the southeastern Superior Province are poor in magmatic sulfate (results above). During ascent of the syn- to late-tectonic arc magmas through the older crust, a substantial amount of sulfate was plausibly lost rather than being entrained during magmatic degassing followed by redox reduction[8,37]. However, the apatite sulfur content peaks, yet is dominated by sulfate, at relatively high zircon $\delta^{18}O$ values of ~6‰ and estimated crustal thickness of ~65 km during the interpreted late-stage subduction and collision (Fig. 2a,b). Hence, we attribute the oxidized sulfur-rich magmas to originate from flux melting of the sub-arc mantle metasomatized by fluids or melts from oceanic crust and the overlying sediments, following the initiation of subduction at ~2,705 Ma (Fig. 3b). The reduction of magmatic $f_{O_2}$ with increasing zircon $\delta^{18}O$ value for the arc magmas is probably caused by enhanced crustal contamination at the source region (for example, from the subducted reduced sediments or lower crustal materials).

The anoxic oceanic environment before 2.7 Ga in the southeastern Superior Province is supported by (1) lower $Fe^{3+}/\Sigma Fe$ ratios of hydrothermally altered oceanic basalts relative to the Phanerozoic equivalents (0.36 ± 0.02 versus 0.52 ± 0.02; 2SE)[15] and (2) low seawater sulfate concentrations (~80 μM) estimated using multiple sulfur isotopes of seafloor ores in volcanogenic massive sulfide deposits[46]. Metamorphic devolatilization of the less oxidized hydrothermally altered seafloor and the overlying sediments is unlikely to release fluids with sufficient oxidized components (for example, $Fe^{3+}$, $S^{6+}$) to metasomatize the mantle[3,5–9,47] from which the widespread oxidized sulfur-rich arc magmas in the southeastern Superior Province were sourced. Rather, it is plausible that the sub-arc mantle source was oxidized (Fig. 3b) by electron transfer via reduction from $H^+$ to $H_2$ in the fluids[48] or hydrogen incorporation in the surrounding mantle (that is, orthopyroxene, or to a lesser extent, olivine and clinopyroxene) coupled with $H_2O$ dissociation[49,50].

Oxidation of the sub-arc mantle via the above two mechanisms requires hydration of the mantle by a large flux of aqueous fluids or hydrous silicate melts released from the subducted hydrated slab lithologies[48–51]. Considering that oxidizing the mantle from the $f_{O_2}$ value of mid-ocean ridge basalts to primitive arc basalts via the mechanism in ref. [48] requires an amount of $H_2O$ three to four orders of magnitude higher than that in refs. [49,50] (with fluid–rock ratios of 1–10 and ~0.002, respectively), we suggest that the latter mechanism is more viable. Release of massive fluid upon slab subduction may readily occur in the Archaean considering (1) the strong capacity of ancient oceanic crust in holding water during hydration[52] and (2) the susceptibility of the oceanic slab to melting upon subduction into the hotter Archaean mantle[21]. We also expect other unconstrained mechanisms, which are out of the scope of this study. Regardless of the exact mechanism involved, the data presented here demonstrate that deep-ocean oxygenation is not a necessary prerequisite for forming oxidized sulfur-rich arc magmas in subduction zones. Note that the interpretation does not preclude the positive role of oxidative seafloor alteration in forming oxidized arc magmas in the Phanerozoic[9].

## Implication for sulfur cycling in early Earth

The switch from submarine to subaerial volcanism is suggested to have fundamentally changed the redox state of volcanic gases during continental stabilization in the Archaean[53,54]. Thermodynamic modelling suggests an increase in S concentrations and $SO_2/H_2S$ ratios of volcanic gases with decreasing pressure[4], the subaerial volcanism can therefore exsolve gases richer in $SO_2$ compared with the submarine counterparts. In contrast, the data presented here document the belt-scale occurrence of oxidized sulfur-rich arc magmas immediately postdating subduction initiation at ~2.7 Ga (Fig. 3b), and many of these magmas formed before the widespread emergence of subaerial landmasses (Fig. 1). Hence, Archaean arc magmas would have emitted $SO_2$-rich volcanic gases to the subaerial and submarine, independent of pressure.

We infer that oxidized sulfur-rich magmas and $SO_2$-rich volcanic emissions may have been common in the late Archaean considering this time was marked by rapid crustal growth and a global initiation of modern-style plate tectonics (evidence summarized in refs. [16,17,21]). The inference is supported by a global appearance of magnetite-series potassic granitoids during syn- to late-tectonic evolution in many Archaean cratons[16,55,56]. Hydrothermal fluids exsolved from the magma chambers may precipitate sulfate veins associated with gold mineralization reported in many Archaean cratons[57]. The volcanic release of $SO_2$-rich gases to the atmosphere would have (1) caused a spike in mass-independent fraction magnitudes at ~2.7 Ga (ref. [58]) and (2) significantly influenced atmospheric $O_2$ concentrations by diminishing $O_2$ sinks[59] and via bacterial sulfate reduction[4,60] owing to exchange of $O_2$ between the atmosphere and seawater.

In conclusion, our results suggest that subduction-zone magmas are oxidized and sulfur-rich independent of ocean redox state. The operation of plate tectonics in the late Archaean may have been instrumental in $SO_2$ outgassing fluxes compared with the associated increase in subaerial volcanism and had a notable influence on magmatic hydrothermal ore formation and oceanic–atmospheric evolution in the Neoarchaean.

## Online content

Any methods, additional references, Nature Portfolio reporting summaries, source data, extended data, supplementary information, acknowledgements, peer review information; details of author contributions and competing interests; and statements of data and code availability are available at https://doi.org/10.1038/s41561-022-01071-5.

## References

1. Edmonds, M. & Wallace, P. J. Volatiles and exsolved vapor in volcanic systems. *Elements* **13**, 29–34 (2017).
2. Wallace, P. J. & Edmonds, M. The sulfur budget in magmas: evidence from melt inclusions, submarine glasses, and volcanic gas emissions. *Rev. Mineral. Geochem.* **73**, 215–246 (2011).
3. Richards, J. P. The oxidation state, and sulfur and Cu contents of arc magmas: implications for metallogeny. *Lithos* **233**, 27–45 (2015).

4. Gaillard, F., Scaillet, B. & Arndt, N. T. Atmospheric oxygenation caused by a change in volcanic degassing pressure. *Nature* **478**, 229–232 (2011).
5. Kelley, K. A. & Cottrell, E. Water and the oxidation state of subduction zone magmas. *Science* **325**, 605–607 (2009).
6. Evans, K. A., Elburg, M. A. & Kamenetsky, V. S. Oxidation state of subarc mantle. *Geology* **40**, 783–786 (2012).
7. Evans, K. A. & Tomkins, A. G. The relationship between subduction zone redox budget and arc magma fertility. *Earth Planet. Sci. Lett.* **308**, 401–409 (2011).
8. Cottrell, E. et al. in *Magma Redox Geochemistry* (eds Moretti, R., & Neuville, D.) 33–61 (John Wiley & Sons, 2021).
9. Stolper, D. A. & Bucholz, C. E. Neoproterozoic to early Phanerozoic rise in island arc redox state due to deep ocean oxygenation and increased marine sulfate levels. *Proc. Natl Acad. Sci. USA* **116**, 8746–8755 (2019).
10. Prouteau, G. & Scaillet, B. Experimental constraints on sulphur behaviour in subduction zones: implications for TTG and adakite production and the global sulphur cycle since the Archean. *J. Petrol.* **54**, 183–213 (2012).
11. Meng, X. et al. Oxidized sulfur-rich arc magmas formed porphyry Cu deposits by 1.88 Ga. *Nat. Commun.* **12**, 2189 (2021).
12. Meng, X. et al. Variable modes of formation for tonalite–trondhjemite–granodiorite–diorite (TTG)-related porphyry-type Cu±Au deposits in the Neoarchean Southern Abitibi Subprovince (Canada): evidence from petrochronology and oxybarometry. *J. Petrol.* https://doi.org/10.1093/petrology/egab079 (2021).
13. Cawood, P. A., Kroner, A. & Pisarevsky, S. Precambrian plate tectonics: criteria and evidence. *GSA Today* **16**, 4–11 (2006).
14. Habicht, K. S., Gade, M., Thamdrup, B., Berg, P. & Canfield, D. E. Calibration of sulfate levels in the Archean ocean. *Science* **298**, 2372–2374 (2002).
15. Stolper, D. A. & Keller, C. B. A record of deep-ocean dissolved $O_2$ from the oxidation state of iron in submarine basalts. *Nature* **553**, 323–327 (2018).
16. Laurent, O., Martin, H., Moyen, J. F. & Doucelance, R. The diversity and evolution of late-Archean granitoids: evidence for the onset of 'modern-style' plate tectonics between 3.0 and 2.5 Ga. *Lithos* **205**, 208–235 (2014).
17. Cawood, P. A. et al. Geological archive of the onset of plate tectonics. *Philos. Trans. R. Soc. A* **376**, 20170405 (2018).
18. Percival, J. A. in *Mineral Deposits of Canada: A Synthesis of Major Deposit-Types, District Metallogeny, the Evolution of Geological Provinces, and Exploration Methods* (ed Goodfellow, W.D.) Special Publication No. 5 903–928 (Geological Association of Canada, Mineral Deposits Division, 2007).
19. Cherniak, D. J. & Watson, E. B. Diffusion in zircon. *Rev. Mineral. Geochem.* **53**, 113–143 (2003).
20. Tang, H., Bell, E. A., Boehnke, P., Barboni, M. & Harrison, T. M. in *AGU Fall Meeting Abstracts* V21B-02 (American Geophysical Union, 2017).
21. Van Hunen, J. & Moyen, J. F. Archean subduction: fact or fiction? *Annu. Rev. Earth Planet. Sci.* **40**, 195–219 (2012).
22. Mole, D. R. et al. The formation of Neoarchean continental crust in the south-east Superior Craton by two distinct geodynamic processes. *Precambrian Res.* **356**, 106104 (2021).
23. Moyen, J. F. & van Hunen, J. Short-term episodicity of Archaean plate tectonics. *Geology* **40**, 451–454 (2012).
24. Beakhouse, G. P. *The Abitibi Subprovince Plutonic Record: Tectonic and Metallogenic Implications* Open File 6268 (Ontario Geological Survey, 2011).
25. Dubé, B. & Mercier-Langevin, P. Gold deposits of the Archean Abitibi greenstone belt. *Can. Soc. Econ. Geol. Spec. Publ.* **23**, 669–708 (2020).
26. Wyman, D. A., Kerrich, R. & Polat, A. Assembly of Archean cratonic mantle lithosphere and crust: plume–arc interaction in the Abitibi–Wawa subduction–accretion complex. *Precambrian Res.* **115**, 37–62 (2002).
27. Chown, E. H., Harrap, R. & Moukhsil, A. The role of granitic intrusions in the evolution of the Abitibi belt, Canada. *Precambrian Res.* **115**, 291–310 (2002).
28. Feng, R. & Kerrich, R. Geobarometry, differential block movements, and crustal, structure of the southwestern Abitibi greenstone belt, Canada. *Geology* **18**, 870–873 (1990).
29. Katz, L. R., Kontak, D. J., Dubé, B. & McNicoll, V. The geology, petrology, and geochronology of the Archean Côté Gold large-tonnage, low-grade intrusion-related Au(–Cu) deposit, Swayze greenstone belt, Ontario, Canada. *Can. J. Earth Sci.* **54**, 173–202 (2017).
30. Beakhouse, G. P. & Davis, D. W. Evolution and tectonic significance of intermediate to felsic plutonism associated with the Hemlo greenstone belt, Superior Province, Canada. *Precambrian Res.* **137**, 61–92 (2005).
31. Piccoli, P. & Candela, P. Apatite in felsic rocks: a model for the estimation of initial halogen concentrations in the Bishop tuff (Long Valley) and Tuolumne intrusive suite (Sierra Nevada batholith) magmas. *Am. J. Sci.* **294**, 92–135 (1994).
32. Hanchar, J. M. & Watson, E. B. Zircon saturation thermometry. *Rev. Mineral. Geochem.* **53**, 89–112 (2003).
33. Ferry, J. M. & Watson, E. B. New thermodynamic models and revised calibrations for the Ti-in-zircon and Zr-in-rutile thermometers. *Contrib. Mineral. Petrol.* **154**, 429–437 (2007).
34. Konecke, B. A., Fiege, A., Simon, A. C., Linsler, S. & Holtz, F. An experimental calibration of a sulfur-in-apatite oxybarometer for mafic systems. *Geochim. Cosmochim. Acta* **265**, 242–258 (2019).
35. Parat, F. & Holtz, F. Sulfur partitioning between apatite and melt and effect of sulfur on apatite solubility at oxidizing conditions. *Contrib. Mineral. Petrol.* **147**, 201–212 (2004).
36. Richards, J. P. Magmatic to hydrothermal metal fluxes in convergent and collided margins. *Ore Geol. Rev.* **40**, 1–26 (2011).
37. Burgisser, A. & Scaillet, B. Redox evolution of a degassing magma rising to the surface. *Nature* **445**, 194–197 (2007).
38. Bell, A. S. & Simon, A. Experimental evidence for the alteration of the $Fe^{3+}/\Sigma Fe$ of silicate melt caused by the degassing of chlorine-bearing aqueous volatiles. *Geology* **39**, 499–502 (2011).
39. Klimm, K., Kohn, S. C. & Botcharnikov, R. E. The dissolution mechanism of sulphur in hydrous silicate melts. II: solubility and speciation of sulphur in hydrous silicate melts as a function of $fO_2$. *Chem. Geol.* **322**, 250–267 (2012).
40. Moretti, R. in *Magma Redox Geochemistry* (eds Moretti, R., & Neuville, D.) 115–138 (John Wiley & Sons, 2021).
41. Tang, M., Lee, C. T. A., Ji, W. Q., Wang, R. & Costin, G. Crustal thickening and endogenic oxidation of magmatic sulfur. *Sci. Adv.* **6**, eaba6342 (2020).
42. Loucks, R. R. Deep entrapment of buoyant magmas by orogenic tectonic stress: its role in producing continental crust, adakites, and porphyry copper deposits. *Earth Sci. Rev.* **220**, 103744 (2021).
43. Laurent, O. et al. Earth's earliest granitoids are crystal-rich magma reservoirs tapped by silicic eruptions. *Nat. Geosci.* **13**, 163–169 (2020).
44. Smithies, R. H. et al. No evidence for high-pressure melting of Earth's crust in the Archean. *Nat. Commun.* **10**, 5559 (2019).
45. Pourteau, A. et al. TTG generation by fluid-fluxed crustal melting: direct evidence from the Proterozoic Georgetown inlier, NE Australia. *Earth Planet. Sci. Lett.* **550**, 116548 (2020).
46. Jamieson, J. W., Wing, B. A., Farquhar, J. & Hannington, M. D. Neoarchaean seawater sulphate concentrations from sulphur isotopes in massive sulphide ore. *Nat. Geosci.* **6**, 61–64 (2013).

47. Ague, J. J. et al. Slab-derived devolatilization fluids oxidized by subducted metasedimentary rocks. *Nat. Geosci.* **15**, 320–326 (2022).
48. Iacovino, K., Guild, M. R. & Till, C. B. Aqueous fluids are effective oxidizing agents of the mantle in subduction zones. *Contrib. Mineral. Petrol.* **175**, 36 (2020).
49. Brandon, A. D. & Draper, D. S. Constraints on the origin of the oxidation state of mantle overlying subduction zones: an example from Simcoe, Washington, USA. *Geochim. Cosmochim. Acta* **60**, 1739–1749 (1996).
50. Tollan, P. & Hermann, J. Arc magmas oxidized by water dissociation and hydrogen incorporation in orthopyroxene. *Nat. Geosci.* **12**, 667–671 (2019).
51. Frost, B. R. & Ballhaus, C. Constraints on the origin of the oxidation state of mantle overlying subduction zones: an example from Simcoe, Washington, USA: comment. *Geochim. Cosmochim. Acta* **62**, 329–331 (1998).
52. Palin, R. M. & White, R. W. Emergence of blueschists on Earth linked to secular changes in oceanic crust composition. *Nat. Geosci.* **9**, 60–64 (2016).
53. Holland, H. D. Volcanic gases, black smokers, and the Great Oxidation Event. *Geochim. Cosmochim. Acta* **66**, 3811–3826 (2002).
54. Kump, L. R. & Barley, M. E. Increased subaerial volcanism and the rise of atmospheric oxygen 2.5 billion years ago. *Nature* **448**, 1033–1036 (2007).
55. Ishihara, S., Ohmoto, H., Anhaeusser, C. R., Imai, A. & Robb, L. J. Discovery of the oldest oxic granitoids in the Kaapvaal Craton and its implications for the redox evolution of early Earth. *Geol. Soc. Am. Mem.* **198**, 67–80 (2006).
56. Moyen, J. F. Archean granitoids: classification, petrology, geochemistry and origin. *Geol. Soc. London Spec. Publ.* **489**, SP489-2018–SP489-22034 (2019).
57. Hattori, K. & Cameron, E. M. Archaean magmatic sulphate. *Nature* **319**, 45–47 (1986).
58. Halevy, I., Johnston, D. T. & Schrag, D. P. Explaining the structure of the archean mass-independent sulfur isotope record. *Science* **329**, 204–207 (2010).
59. Meixnerová, J. et al. Mercury abundance and isotopic composition indicate subaerial volcanism prior to the end-Archean 'whiff' of oxygen. *Proc. Natl Acad. Sci. USA* **118**, e2107511118 (2021).
60. Olson, S. L. et al. Volcanically modulated pyrite burial and ocean–atmosphere oxidation. *Earth Planet. Sci. Lett.* **506**, 417–427 (2019).
61. Frieman, B. M., Kuiper, Y. D., Kelly, N. M., Monecke, T. & Kylander-Clark, A. Constraints on the geodynamic evolution of the southern Superior Province: U–Pb LA-ICP-MS analysis of detrital zircon in successor basins of the Archean Abitibi and Pontiac subprovinces of Ontario and Quebec, Canada. *Precambrian Res.* **292**, 398–416 (2017).
62. Loucks, R. R., Fiorentini, M. L. & Henríquez, G. J. New magmatic oxybarometer using trace elements in zircon. *J. Petrol.* **61**, egaa034 (2020).
63. Valley, J. W., Kinny, P. D., Schulze, D. J. & Spicuzza, M. J. Zircon megacrysts from kimberlite: oxygen isotope variability among mantle melts. *Contrib. Mineral. Petrol.* **133**, 1–11 (1998).
64. Smithies, R. H. et al. Oxygen isotopes trace the origins of Earth's earliest continental crust. *Nature* **592**, 70–75 (2021).

**Publisher's note** Springer Nature remains neutral with regard to jurisdictional claims in published maps and institutional affiliations.

Springer Nature or its licensor (e.g. a society or other partner) holds exclusive rights to this article under a publishing agreement with the author(s) or other rightsholder(s); author self-archiving of the accepted manuscript version of this article is solely governed by the terms of such publishing agreement and applicable law.

© The Author(s), under exclusive licence to Springer Nature Limited 2022

# Methods

## Sample preparation

We mounted ~6,000 zircon grains from 93 intrusive samples across the southeastern Superior Province (mainly from the Abitibi–Wawa greenstone belt; Extended Data Fig. 1). These samples have previously been dated, and the zircon Hf–O isotopes were reported[22]. We used a Tescan Vega 3 scanning electron microscope equipped with a Bruker energy-dispersive spectrometer at Laurentian University to identify the mineral inclusions. Various types and numbers of mineral inclusions were exposed and identified in the zircon samples, including apatite, quartz, K-feldspar, plagioclase and minor biotite, amphibole, rutile, titanite and Fe–Ti oxides. Apatite is the most common type of mineral inclusion. The intrusive samples that contain the exposed apatite inclusions include (1) 21 samples of syn-volcanic tonalite–trondhjemitic rocks, (2) 11 samples of early syn-tectonic tonalite–granodiorite and (3) 18 samples of syn- to late-tectonic potassic rocks (including sanukitoid and alkalic rocks). A magnetite–ilmenite mineral pair has not been found in the zircon samples. The Fe–Ti oxide minerals are rarely exposed, including three ilmenite inclusions in pre-tectonic TTG rocks (samples LAP-2, 92HNB-0070C and SJ-04) and two magnetite inclusions in the syn- to late-tectonic TTG and potassic rocks (samples OP242 and ZB93-416AZ).

To minimize any potential effects from metamorphism and hydrothermal alteration, we restrict to analyse the zircon-hosted apatite inclusions that are remote from fractures. All of these zircon grains have oscillatory or sector zonings as shown in backscattered electron (BSE) and cathodoluminescence (CL) images (this study and ref. [22]; Extended Data Fig. 2). Zircon xenocryst cores are distinguished from the rims by an irregular geometrical surface and have been verified using the U–Pb dating results reported in ref. [22]. To minimize the effect of crustal contaminants during magma ascent on the magmatic $f_{O_2}$ and composition, samples with abundant zircon xenocrysts have been excluded. Note that a few samples with abundant zircon antecrysts (that is, formed from earlier pulses of magma from the source, yielding distinct petrographic features but identical $^{207}Pb/^{206}Pb$ dates and Hf–O isotope values with the rims) have been included because the magmatic parameters are not expected to significantly change over the short period of time.

## EPMA

The major and trace elements of the apatite inclusions were acquired with a Cameca SX100 electron microprobe analyser operated using the wavelength-dispersive spectrometry method at the Ontario Geoscience Laboratories (GeoLabs). Fourteen elements (P, Si, Al, Mg, Ca, Mn, Fe, Sr, Na, K, S, F, Cl, Zr) were measured using the following conditions: 15 kV accelerating voltage, 10 nA beam current and 2 µm or 5 µm raster beam sizes. X-ray lines, analysing crystals, counting times (for both peak and background measurements) were as follows: P Kα, LPET5, 15 s; Si Kα, LTAP2, 20 s; Al Kα, LTAP2, 20 s; Mg Kα, LTAP2, 20 s; Ca Kα, LPET5, 15 s; Mn Kα, LiF4, 40 s; Fe Kα, LiF4, 40 s; Sr Lα, LPET5, 30 s; Na Kα, LTAP2, 20 s; K Kα, PET3, 20 s; S Kα, LPET3, 60 s; F Kα, PCO, 5 s; Cl Kα, LPET5, 20 s; Zr Lα, LPET5, 5 s. The detection limits for these elements were calculated to be as follows: $P_2O_5$, 930 ppm; $SiO_2$, 210 ppm; $Al_2O_3$, 190 ppm; MgO, 200 ppm; CaO, 480 ppm; MnO, 930 ppm; FeO, 770 ppm; SrO, 1,230 ppm; $Na_2O$, 250 ppm; $K_2O$, 210 ppm; $SO_3$, 310 ppm; F, 1,850 ppm and Cl, 250 ppm.

Zirconium concentrations were measured to monitor the contamination of the apatite by the host zircon; analyses with >1 wt% $ZrO_2$ were excluded. As apatite is prone to decomposition due to electron beam damage, the resultant effect on halogen content was tested. As previously reported in ref. [11], the S and Cl contents have been tested to be reliable, but F content in apatite (~20 s) may be compromised by decomposition using a 2 µm beam. During our analyses, we used a 5 s acquisition for F to minimize the decomposition, but the precision for the F may be affected. Damage of apatite using a beam size of 5 µm can be minimized, particularly for apatite grains with the *c*-axis perpendicular to the electron beam. The test results were taken into account for analysis and data screening.

## Micro X-ray absorption near-edge structure at the S K-edge

Micro X-ray absorption near-edge structure spectroscopy at the sulfur K-edge (S µ-XANES) was conducted to measure the sulfur oxidation states of apatite inclusions at the Advanced Photon Source of the Argonne National Laboratory in Chicago, Illinois, USA. Details of the method in analysing zircon-hosted apatite inclusions are in ref. [11]. The µ-XANES analyses were conducted on representative apatite crystals unaffected by prior electron microprobe beam analysis. Two scans were collected at each point to improve counting statistics and to monitor for beam damage caused by irradiation of the focused X-ray beam and contribution from other phases (for example, the host zircon, epoxy). Beam damage was not observed in any apatite spectra collected in this study, consistent with previous observations that apatite does not easily incur beam damage at the energies for S µ-XANES analyses even after 1 hour of beam exposure[34]. Contributions of zircon and sulfur-bearing epoxy to the S µ-XANES spectra were monitored following the criteria described in refs. [11,34], and any spectra with contamination from other phases were discarded. The S µ-XANES spectra on the same apatite grain were normalized and merged using the X-ray absorption spectroscopy (XAS) software analysis package Athena or Ifeffit[65]. Peak positions and areas were then fitted and calculated using the Fityk software version 1.3.1 (ref. [66]), from which the integrated $S^{6+}$ / ΣS peak area ratios were calculated and used for estimating $f_{O_2}$ values at the time of apatite crystallization.

## Methods in estimating the crustal thickness

The La/Yb ratios of the intermediate-felsic rocks were used to estimate the crustal thickness following the method in ref. [67], that is, crustal thickness (km) = 21.277 × ln(1.0204 × La/Ybn). The La/Ybn represents the chondrite-normalized La/Yb ratio in which the normalization values are from ref. [68]. The whole-rock geochemistry data were compiled in ref. [22] from online public datasets, including (1) GEOROC online database[69]; (2) Ontario Geological Survey miscellaneous-release data MRD285 (ref. [24]), MRD143 (ref. [70]), MRD282 (ref. [71]) and (3) Ministère des Ressources Naturelles du Québec online dataset (SIGEOM). The compiled datasets have been classified[22], and we used only the whole-rock geochemistry data for the TTG, potassic and sanukitoid intrusive rocks with accurate coordinates. The recently published lithogeochemistry data[12] were also included.

As rare earth elements, La and Yb are relatively fluid-immobile and are therefore resistant to post-crystallization metamorphism and alteration[72]. However, high-temperature melting can strongly elevate La versus Yb contents[73], and the late-stage magma differentiation may affect the La/Yb ratios. In both situations, the crustal thickness will be inaccurately estimated. We therefore filtered the data using criteria as follows: (1) loss on ignition (LOI) ≤ 5 wt% (ref. [44]), (2) 55 wt% ≤ $SiO_2$ ≤ 68 wt% (ref. [67]), (3) 1 ≤ MgO ≤ 6 wt% (ref. [67]), (4) La ≤ 70 ppm (ref. [73]). The $SiO_2$, MgO and La contents were calculated on the anhydrous basis. Furthermore, the data for the sodic TTG rocks were filtered to remove those with $K_2O/Na_2O \geq 0.6$, whereas the data for the syn- to late-tectonic potassic rocks with $K_2O/Na_2O < 0.6$ were excluded[44]. We also excluded two of the potassic samples with A/CNK (mole $Al_2O_3$/($CaO+Na_2O+K_2O$)) > 1.1, which are possibly S-type granite[74].

Using the filtering criteria, we obtained 773 and 135 data points for the sodic TTG and potassic rocks (including sanukitoid), respectively (Extended Data Figs. 1 and 6). Previous studies suggest that most TTG rocks formed before 2,685 Ma followed by extensive emplacement of sanukitoid and potassic rocks[25]. The sanukitoid samples are included in the lithogeochemical dataset for the potassic rocks because most formed in syn- to late-tectonic stages. The crust in the southeastern Superior Province (mainly Abitibi–Wawa belt) thickened on average

from 48 ± 21 km (σ, $n$ = 773) to 65 ± 14 km (σ, $n$ = 135) as a result of collision (Extended Data Fig. 6). We used ArcGIS Pro to illustrate the crustal thickness via the empirical Bayesian Kriging model and predict the crustal thickness at which our studied samples were collected. The standard errors for the predicted crustal thickness are also calculated. Most of our studied samples are close to the data points involved in predicting the crustal thickness except for a few samples in the Wawa greenstone belt (Extended Data Fig. 1).

### P–T correction of magmatic $f_{O_2}$ estimated from S in apatite oxybarometer

We use the S in apatite oxybarometer[34] to estimate magmatic $f_{O_2}$ values for the arc magmas formed <2,705 Ma in the southeastern Superior Province. Zircon grains from the pre-tectonic TTG rocks yielded lower Eu/Eu* ratios (0.31 ± 0.06, 2SE) than those from the syn-tectonic TTG (0.49 ± 0.09, 2SE) and syn- to late-tectonic TTG rocks (0.55 ± 0.08, 2SE), which may, in part, be caused by depletion of Eu by plagioclase fractionation[75] in the pre-tectonic TTG magmas. Early plagioclase fractionation commonly occurs in relatively dry magma[76] (for example, sourced from thin crust[75]). In dry magma, the sulfide–sulfate transition may shift to relatively reduced $f_{O_2}$ space, but the extent remains poorly calibrated[40]. The S in apatite oxybarometer is therefore not used for the pre-tectonic rocks.

In silicate melt, a decrease in temperature of 100 °C and pressure of 300 MPa have experimentally been suggested to result in a deviation of ΔFMQ + 0.5 and −0.2, respectively[77,78]. Considering the effect of temperature and pressure on silicate melt is proportional to the effect of sulfur incorporation into apatite, we evaluated the pressure and temperature at which the zircon-hosted apatite inclusions crystallized to correct the magmatic $f_{O_2}$ estimated from the S in apatite oxybarometer.

The emplacement pressures for rocks with appropriate mineral assemblages (hornblende + biotite + plagioclase + quartz + alkali feldspar + Fe–Ti oxide) were estimated using the Al in amphibole barometers. We summarized the previously published results as follows. (1) The syn-tectonic TTG and sanukitoid rocks were mainly constrained to emplace at 200–400 MPa (refs. [12,24,30]). (2) The late-tectonic stocks (that is, Otto and Garrison stocks) have been estimated to be emplaced at ~100 MPa (ref. [28]). We used these results as the emplacement pressures for our samples.

Apatite saturation thermometry is employed to estimate the temperature at which the apatite began to crystallize[31]. Considering the apatite may crystallize in near-liquidus condition, we calculated the *modelled* apatite saturation temperature using whole-rock $SiO_2$ and $P_2O_5$ contents on an anhydrous basis[79]. Because the apatite saturation thermometer is more suitable for metaluminous to slightly peraluminous systems[31] and the $SiO_2$ and $P_2O_5$ may be affected by hydrothermal alteration, we filtered the previously compiled geochemical dataset using the following criteria: A/CNK (mole $Al_2O_3/(CaO+Na_2O+K_2O)$) ≤ 1.1 and LOI < 2.5 wt%. We further subdivided the dataset into three groups of rocks with different composition: sodic TTG rocks, potassic rocks and sanukitoids, and their modelled apatite saturation temperatures are comparable with uncertainties at 898 ± 50 °C (σ, $n$ = 1,924; Extended Data Fig. 3), 896 ± 69 °C (σ, $n$ = 460; Extended Data Fig. 3), and 920 ± 45 °C (σ, $n$ = 38; Extended Data Fig. 3), respectively. Note that some of the potassic rocks are probably derivative sanukitoid, and the average value for all of these rocks is 898 ± 54 °C (σ, $n$ = 2,422).

## Data availability

The data that support the findings of this study are available at https://doi.org/10.5281/zenodo.7151046.

## References


65. Ravel, B. & Newville, M. ATHENA, ARTEMIS, HEPHAESTUS: data analysis for X-ray absorption spectroscopy using IFEFFIT. *J. Synchrotron Radiat.* **12**, 537–541 (2005).
66. Wojdyr, M. Fityk: a general-purpose peak fitting program. *J. Appl. Crystallogr.* **43**, 1126–1128 (2010).
67. Profeta, L. et al. Quantifying crustal thickness over time in magmatic arcs. *Sci. Rep.* **5**, 17786 (2015).
68. Sun, S. S. & McDonough, W. F. Chemical and isotopic systematics of oceanic basalts: implications for mantle composition and processes. *Geol. Soc. Lond. Spec. Publ.* **42**, 313–345 (1989).
69. Sarbas, B. & Nohl, U. The GEOROC database as part of a growing geoinformatics network. *Geoinformatics* 2008—Data to Knowledge, Proceedings. 42–43 (Potsdam, 2008).
70. Ayer, J. A., Trowell, N. F. & Josey, S. *Geological Compilation of the Abitibi Greenstone Belt* Miscellaneous Release—Data 143 (Ontario Geological Survey, 2004).
71. Ayer, J. A. & Chartrand, J. E. *Geological Compilation of the Abitibi Greenstone Belt* Miscellaneous Release—Data 282 (Ontario Geological Survey, 2011).
72. Bau, M. Rare-earth element mobility during hydrothermal and metamorphic fluid-rock interaction and the significance of the oxidation state of europium. *Chem. Geol.* **93**, 219–230 (1991).
73. Hu, F. et al. Quantitatively tracking the elevation of the Tibetan Plateau since the Cretaceous: insights from whole-rock Sr/Y and La/Yb ratios. *Geophys. Res. Lett.* **47**, e2020GL089202 (2020).
74. Clarke, D. B. The mineralogy of peraluminous granites; a review. *Can. Mineralogist* **19**, 3–17 (1981).
75. Tang, M., Ji, W. Q., Chu, X., Wu, A. & Chen, C. Reconstructing crustal thickness evolution from europium anomalies in detrital zircons. *Geology* **49**, 76–80 (2020).
76. Richards, J. P. High Sr/Y arc magmas and porphyry Cu ± Mo ± Au deposits: just add water. *Econ. Geol.* **106**, 1075–1081 (2011).
77. Matjuschkin, V., Blundy, J. D. & Brooker, R. A. The effect of pressure on sulphur speciation in mid- to deep-crustal arc magmas and implications for the formation of porphyry copper deposits. *Contrib. Mineral. Petrol.* **171**, 1–25 (2016).
78. Nash, W. M., Smythe, D. J. & Wood, B. J. Compositional and temperature effects on sulfur speciation and solubility in silicate melts. *Earth Planet. Sci. Lett.* **507**, 187–198 (2019).
79. Piccoli, P. M. & Candela, P. A. Apatite in igneous systems. *Rev. Mineral. Geochem.* **48**, 255–292 (2002).
80. Montsion, R., Thurston, P. & Ayer, J. *1:2,000,000 Scale Geological Compilation of the Superior Craton* Version 1 (Mineral Exploration Research Centre, Harquail School of Earth Sciences, Laurentian University, 2018).


## Acknowledgements


The research was funded by Canada First Research Excellence Fund via a Metal Earth (CFREF-2015-00005) thematic project to J.P.R., the National Natural Science Foundation of China (grant number 41820104010, J.M.), the US National Science Foundation EAR (grant number 1924192, A.C.S.) and a China Scholarship Council Ph.D. scholarship (X.M.). We thank D. Crabtree at Ontario GeoLabs for assistance in electron microprobe analysis and A. Lanzirotti and M. Newville at Advanced Photon Sources in the United States for μ-XANES analysis. The research used synchrotron resources (Sector 13-ID-E) of Advanced Photon Source in Argonne National Laboratory under contract number DE-AC02-06CH11357. We thank the Geological Survey of Canada, Ontario Geological Survey, Jack Satterley Geochronology Laboratory (University of Toronto), Ministère de l'Énergie et des Ressources Naturelles and the Centre de recherche sur la dynamique du système Terre (GEOTOP; University of Quebec at Montreal) for provision of sample materials. This is a contribution of MERC-ME-2022-31 from Mineral Exploration Research Centre, Harquail School of Earth Sciences.


## Author contributions

X.M. conceived the project and wrote the first version of the manuscript. J.P.R. assisted X.M. in designing an initial project.

X.M. identified and measured the composition of the zircon-hosted apatite inclusions and worked with A.C.S. and J.M.K. to complete the μ-XANES analysis. D.R.M. mounted the zircon grains that were previously used for the Hf–O isotopic mapping project of the southeastern Superior Province. All of the authors, including J.M., D.J.K. and P.J.J. contributed to interpreting the data and revising the manuscript.

## Competing interests

The authors declare no competing interests.

## Additional information

**Extended data** is available for this paper at https://doi.org/10.1038/s41561-022-01071-5.

**Supplementary information** The online version contains supplementary material available at https://doi.org/10.1038/s41561-022-01071-5.

**Correspondence and requests for materials** should be addressed to Xuyang Meng, Adam C. Simon or Jingwen Mao.

**Peer review information** *Nature Geoscience* thanks the anonymous reviewers for their contribution to the peer review of this work. Primary Handling editor: Rebecca Neely, in collaboration with the *Nature Geoscience* team.

**Reprints and permissions information** is available at www.nature.com/reprints.

https://doi.org/10.1038/s41561-022-01071-5

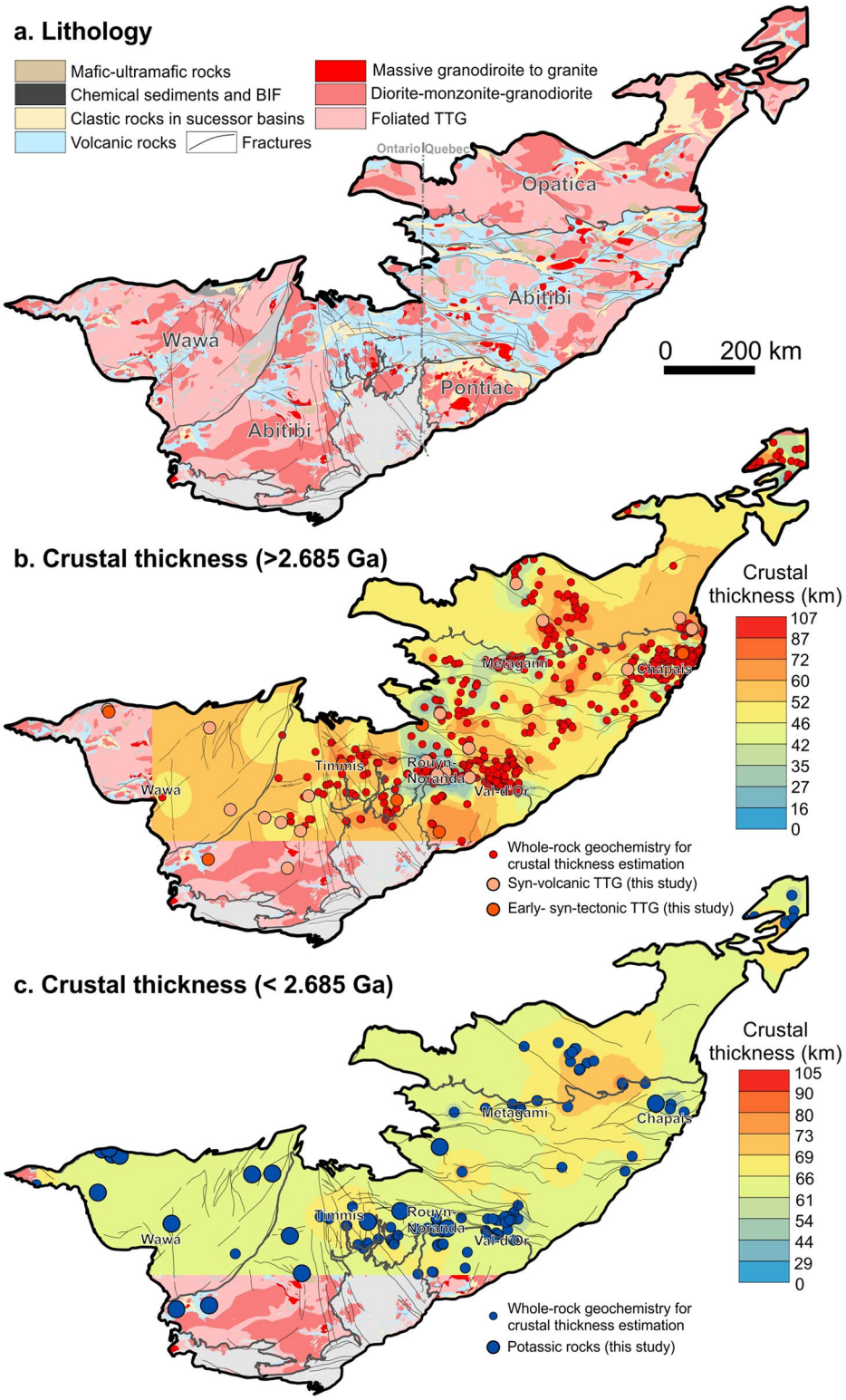


**Extended Data Fig. 1 | Simplified geological map of the southeastern Superior Province[80] and the spatial distribution of the estimated crustal thickness.** **a**, Lithology; **b**, Crustal thickness at >2.685 Ga; **c**, Crustal thickness at <2.685 Ga. See crustal thickness estimation in the 'Methods' section.

https://doi.org/10.1038/s41561-022-01071-5

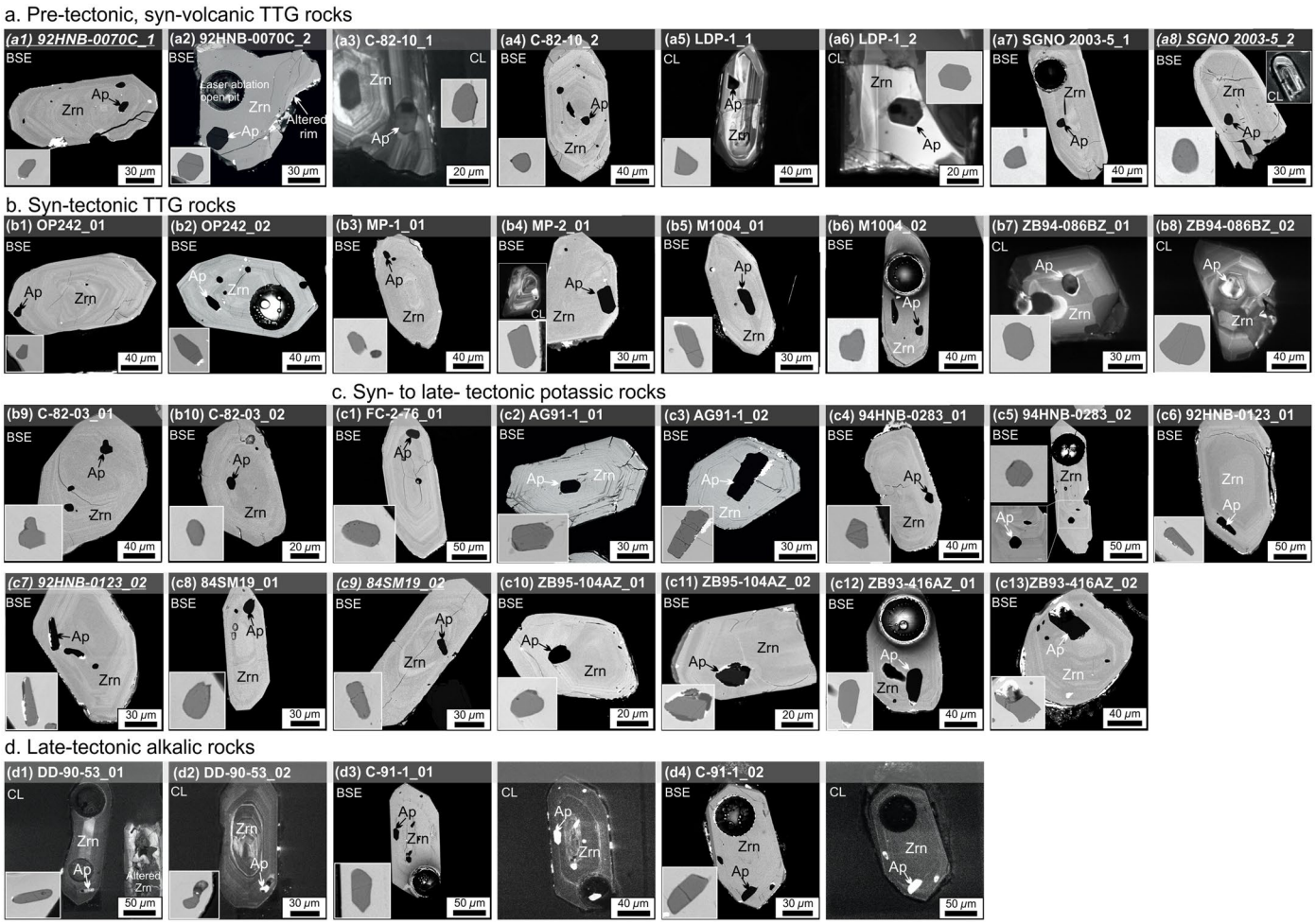


**Extended Data Fig. 2 | Backscattered electron or cathodoluminescence images of zircons with apatite inclusions used for $\mu$-XANES analyses that were separated from representative granitoid rocks from the southeastern Superior Province.** The samples have been grouped into (**a**) pre-tectonic, syn-volcanic TTG rocks; (**b**) syn-tectonic TTG rocks; (**c**) syn- to late-tectonic potassic rocks including (**d**) late-tectonic alkalic rocks. Insets are mainly BSE images for the analyzed apatite inclusions with a few CL images for the zircon hosts (a8 and b4). Note that the low S concentrations in apatite inclusions in a1 and a8 make the S-XANES spectra undetectable, whereas spectra for the apatite inclusions in c7 and c9 have been contaminated by the zircon hosts and were excluded. Abbreviations: Ap = apatite, Zrn = zircon. See sample information in Supplementary Table 1.

https://doi.org/10.1038/s41561-022-01071-5

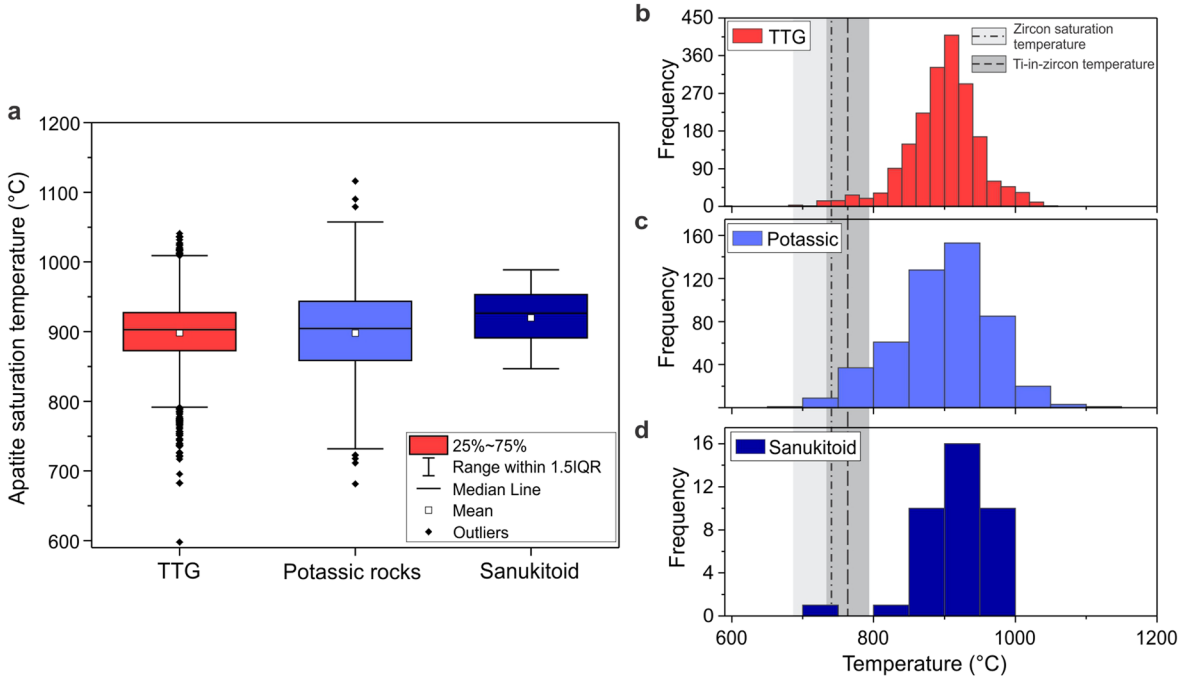


**Extended Data Fig. 3 | Box charts and histograms for the calculated apatite saturation temperatures estimated for TTG (in red; 898 ± 50 °C, 1σ, n = 1924), potassic (in light blue; 896 ± 69 °C, 1σ, n = 460), and sanukitoid (in blue; 920 ± 45 °C, 1σ, n = 38) rocks in the southeastern Superior Province.** The average values of Ti-in-zircon (764 ± 30 °C, 1σ, n = 50) and zircon saturation temperatures (741 ± 54 °C, 1σ, n = 50, n = 1822) for all of the available samples are calculated and plotted for comparison. The zircon saturation temperature and Ti-in-zircon temperature are calculated using methods of ref. [32] and ref. [33], respectively. Box-and-whisker plots in (a) indicate the median, first and third quartiles, and lower to upper whiskers (±1.5×interquartile range). IQR = interquartile range. The square dots and black diamonds represent mean values and outliers, respectively. The error bands for the zircon saturation and Ti-in-zircon temperatures in (b-d) represent standard deviations.

https://doi.org/10.1038/s41561-022-01071-5

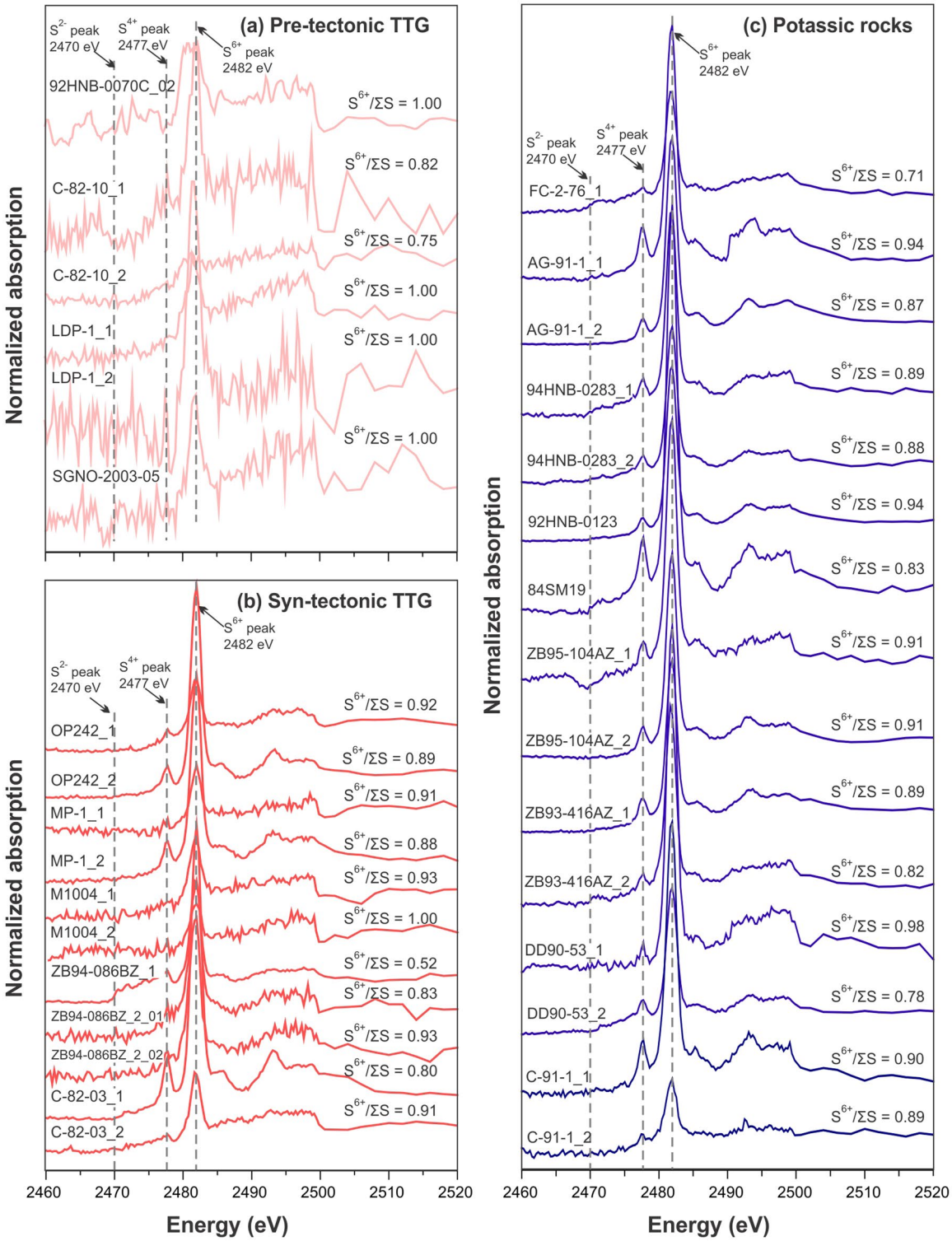


**Extended Data Fig. 4 | Normalized apatite $\mu$-XANES spectra at S *K*-edge for representative intermediate-felsic rocks from the southeastern Superior Province (Canada). a**, pre-tectonic TTG (in pink). **b**, syn-tectonic TTG (in red). **c**, potassic rocks (in blue). The analysis numbers are consistent with the sample numbers in Extended Data Fig. 2. Peak positions for $S^{2-}$, $S^{4+}$, $S^{6+}$ are at 2470 eV, 2477 eV, and 2482 eV, respectively, and are shown as dotted gray lines. The calculated $S^{6+}/\Sigma S$ ratios are shown on right of each spectra. See sample information in Supplementary Table 1.

https://doi.org/10.1038/s41561-022-01071-5

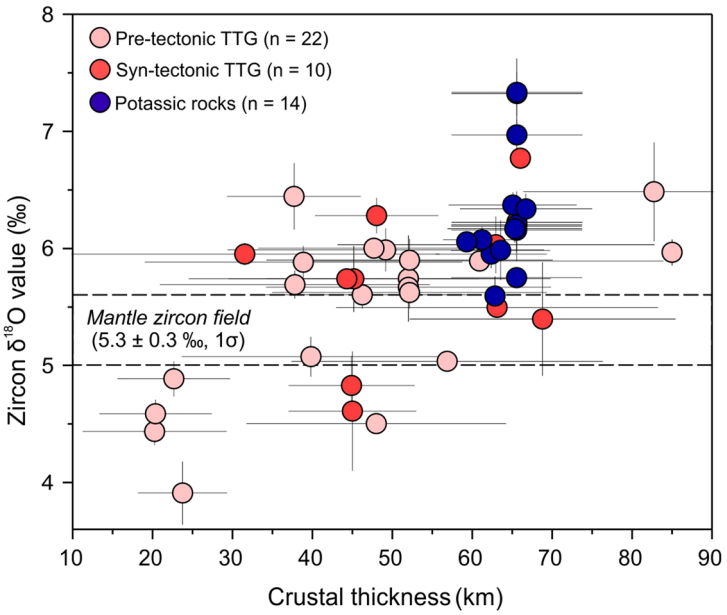


**Extended Data Fig. 5 | Plot of the estimated crustal thickness versus zircon $\delta^{18}O$ values.** The zircon O isotopic data for sodic and potassic rocks are from ref. [12,22]. The mantle value for zircon O isotopes is from ref. [63]. Error bars indicate 1σ uncertainties. N represents numbers of rock samples.

https://doi.org/10.1038/s41561-022-01071-5

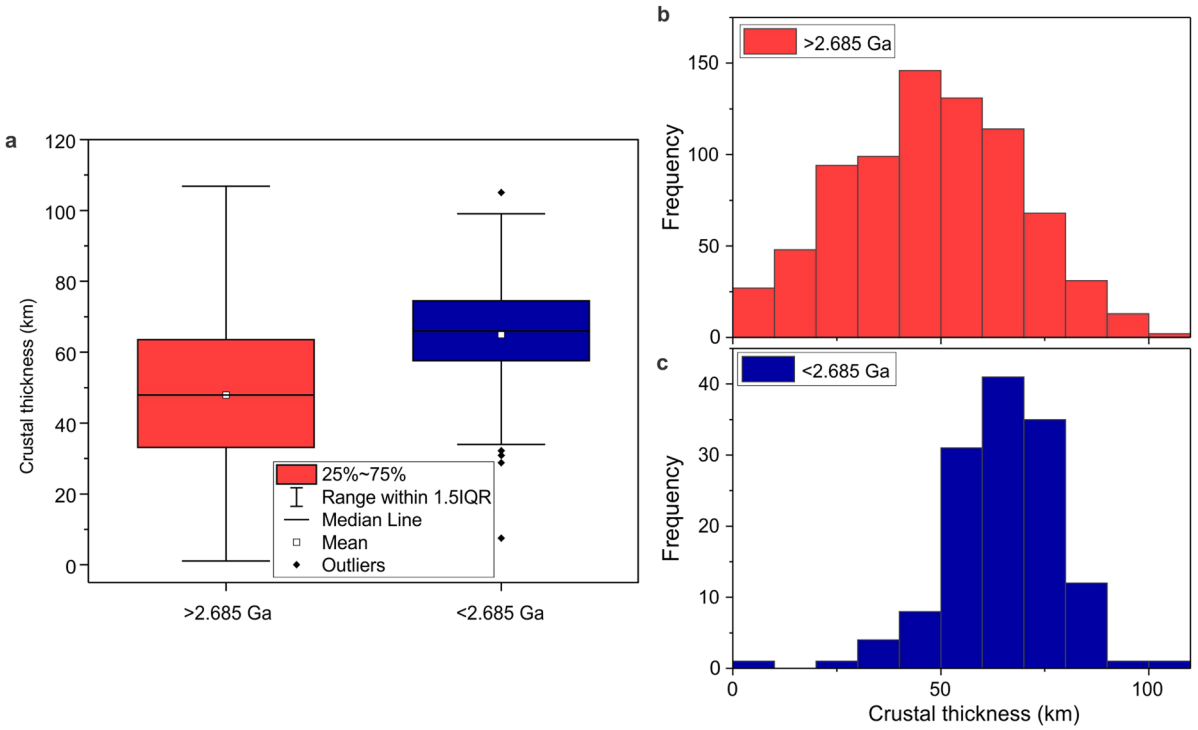


**Extended Data Fig. 6 | Box charts and histograms for the crustal thickness of southeastern Superior Province at >2.685 Ga and <2.685 Ga estimated based on compositions of TTG (in red; 48 ± 21 km, 1σ, n = 773) and potassic (including sanukitoid, in blue; to 65 ± 14 km, 1σ, n = 135) rocks, respectively.** Box-and-whisker plots in (a) indicate the median, first and third quartiles, and lower to upper whiskers (±1.5×interquartile range). IQR = interquartile range. The square dots and black diamonds represent mean values and outliers, respectively.